Nano Research

ISSN 1998-0124 CN 11-5974/O4

https://doi.org/10.1007/s12274-019-2576-4

Research Article

Highly graphitized carbon nanosheets with embedded Ni nanocrystals as anode for Li-ion batteries

Francisco Javier Soler-Piña[1], Celia Hernández-Rentero[1], Alvaro Caballero[1] (✉), Julián Morales[1] (✉), Enrique Rodríguez-Castellón[2], and Jesús Canales-Vázquez[3]

[1] *Dpto. Química Inorgánica e Ingeniería Química, Instituto de Química Fina y Nanoquímica, Universidad de Córdoba, 14071 Córdoba, Spain*

[2] *Dpto. Química Inorgánica, Cristalografía y Mineralogía, Facultad de Ciencias, Universidad de Málaga, 29071 Málaga, Spain*

[3] *Instituto de Energías Renovables, Universidad de Castilla-La Mancha, Paseo de La Investigación 1, 02071 Albacete, Spain*

Received: 15 July 2019 / **Revised:** 20 November 2019 / **Accepted:** 23 November 2019

ABSTRACT

A C/Ni composite was prepared via thermal decomposition of a nickel oleate complex at 700 °C, yielding disperse Ni nanocrystals with an average size of 20 nm, encapsulated by carbon nanosheets as deduced from transmission electron microscopy (TEM) images and confirmed from X-ray photoelectron spectroscopy (XPS). Furthermore, the X-ray diffraction pattern revealed a good ordering of the carbon layers, forced by the Ni encapsulation to adopt a bending structure. Considering the close interaction between the graphitized framework and the metallic nanoparticles we have studied the properties of the composite as an anode for Li-ion batteries. Compared with other nanostructured synthetic carbons, this carbon composite has a low voltage hysteresis and a modest irreversible capacity value, properties that play a significant role in its behaviour as electrodes in full cell configuration. At moderate rate values, 0.25 C, the electrode delivers an average capacity value around 723 mAh·g^{-1} on cycling, among the highest values so far reported for this carbon type. At higher rate values, 1 C, the average capacity values delivered by the cell on cycling decrease, around 205 mAh·g^{-1}, but it maintains good capacity retention, a coulombic efficiency close to 100% after the first cycles and recovery of the capacity values when the rate is restored from 3 to 0.1 C.

KEYWORDS

carbon nanosheets, nickel nanoparticles, anode, lithium batteries

1 Introduction

Monodisperse nanoparticles based on transition metals have received great attention both due to their scientific interest and their multiple applications [1–3]. Given the extraordinary tendency of these nanostructured systems to agglomerate, a proper choice of the synthesis method is a key requirement to mitigate it. Among the different available methods [4, 5], special attention has been given to the one based on the thermal decomposition of transition metal-carboxilates complexes (including fatty acid salts), first reported by Park et al. [6] and Jana et al. [7] for obtaining, Cr, Mn, Fe, Co and Ni oxides nanocrystals and further applied to mixed oxides and other transition elements [8–18]. The oxide formation or the element itself has been related to the Gibbs formation energy of metal oxide (ΔG^0) and electronegativity (χP) [11]. High values of ΔG^0 and low values of χP would justify the formation of the oxide from the thermal decomposition of the oleate (Cr, Mn). The decomposition of the oleates of more electronegative elements such as Co, Ni, and Cu, whose oxides have lower free energies of formation would lead to the formation of the elements themselves. Fe is in an intermediate position; hence the decomposition product can be a mixture of oxide and metal [6]. The model fails when applied to the Co element since it has also been found that the thermal decomposition of Co (II) oleate can lead to the formation of wurzite-type CoO nanocrystals [13]. The thermal decomposition of Ni [10, 11, 14, 15] and Cu [8] oleates whose oxides have slightly lower Gibbs energies adapt to the model.

To obtain monodisperse and self-assembled nanocrystals, the strategy used is to add a surfactant agent, for example oleic acid, which is anchored on its surface. The removal of nanocrystals by chemical procedures and further calcination could lead to an ordered mesoporous carbon (OMC) with interesting applications in the field of electrochemical energy storage devices. Dong et al. have paid special attention to Fe_3O_4 nanocrystals and the resulting OMCs have been tested as electrodes in Li-ion [16], Li/S batteries [17] and supercapacitors [18] with outstanding results. This application for the carbon matrix could also be examined without the need to remove the nanocrystals, which is the objective of this work. Herein, the metal-oleate-oleic acid system is pyrolyzed under inert atmosphere after heating. Under these conditions, the nanocrystals are coated with a carbon film whose degree of graphitization depends on the element present in the nanocrystals. As precursor of nanocrystals we have chosen the Ni oleate for two main reasons. First, the thermal decomposition of this oleate produces nanoparticles of Ni metal [10, 11, 14, 15] whose conductive properties would decrease the resistance of the electrode. Second, it is well known that Ni catalyzes, among other processes, the degree of graphitization of synthetic carbons [19]. This parameter has special relevance since the carbons with high structural disorder have high values

Address correspondence to Alvaro Caballero, alvaro.caballero@uco.es; Julián Morales, iq1mopaj@uco.es

of the irreversible capacity as observed in the aforementioned OMCs [16].

2 Materials and methods

2.1 Synthesis of Ni(II)-oleate-oleic acid system

The nickel-oleate complex was prepared from $NiCl_2{\cdot}6H_2O$ and excess of $Na(C_{18}H_{33}O_2)$. In a round bottom flask, 9.5 g of nickel (II) chloride and 36.5 g of sodium oleate were mixed with 80 mL of ethanol, 60 mL of distilled water and 140 mL of hexane. Then, a reflux was carried out at 70 °C in a polyethylene glycol bath for 4 h, while controlling the temperature of the system with a thermocouple. The mixture obtained has two phases: One is aqueous and the other is organic, less dense and green due to the presence of nickel (II) complex. The aqueous phase was discarded, using a separatory funnel. Subsequently, the organic phase was washed 3 times with distilled water with the purpose of removing sodium cations and ethanol. Finally, the hexane contained in the organic phase was evaporated in a Petri dish at room temperature for 4–5 days. The complex has the appearance of a green waxy solid.

In the next step, 21 g of the Ni complex were dissolved in 3.7 mL of oleic acid and 148 mL of 1-octadecene at room temperature. The solution was heated under N_2 atmosphere at 320 °C for half an hour under reflux, using a 3.3 °C·min^{-1} ramp. The viscosity of the solution increased, and its green color became darker. After this treatment, the mixture was cooled to a temperature below 200 °C in an inert atmosphere. Then, the nitrogen flow was cut off when the risk of 1-octadecene combustion disappeared. After cooling, 500 mL of ethanol were added as the washing liquid. The dark green emulsion was separated from the supernatant by centrifugation at 4,000 rpm for 20 min. Finally, the emulsion was dried at 100 °C for 2 days, forming black crystals that, when grounded in a mortar, were transformed into a waxy yellow solid (WYS). This solid was calcined at 500 and 700 °C under N_2 atmosphere for 4 h using a heating rate of 5 °C·min^{-1}. These samples will be designated C/Ni500 and C/Ni700, respectively. The synthesis pathway of the samples from oleate salts is schematically described in Fig. 1.

2.2 Characterization techniques

X-ray diffraction patterns (XRD) were obtained with a Bruker D8 Discover X-ray diffractometer using monochromatic Cu Kα radiation. The patterns were observed in the 5°–80° (2θ) range, using a step size of 0.040° and 1.05 s per step. The Raman spectra were recorded under ambient conditions using a Renishaw in Via Microscope equipped with a detector Renishaw CCD Camera (578 × 400) and a laser of 532 nm edge in line focus mode. X-ray photoelectron spectroscopy (XPS) measurements were carried out with a Physical Electronics PHI 5700 spectrometer using monochromatic Mg Kα radiation and a multichannel detector. The nitrogen adsorption/desorption data were obtained at liquid nitrogen temperature (77 K) using a Micromeritics ASAP 2020 M apparatus. Thermogravimetric measurements were made using a Mettler Toledo-TGA/DSC. TEM images were obtained with a JEOL 2100 electron microscope operating at 200 kV and equipped with an Orius Gatan CCD camera.

2.3 Electrochemical measurements

The working electrodes were prepared by mixing the active material with poly(vinylidene difluoride) (PVDF) (Fluka) and carbon super P (Timcal) in a weight proportion of 80:10:10 and adding 1-methyl-2-pyrrolidinone (Sigma-Aldrich) to obtain a slurry which was spreaded on gas diffusion layer (GDL, SGL Group) carbon substrate with the help of doctor-blade method. The carbon loading was 4.2 mg·cm^{-2}. Their electrochemical performance was tested in two electrode CR2032 coin cells with Li foil as counter electrode. The electrolyte was 1 M $LiPF_6$ dissolved in a 1:1 (w/w) mixture of ethylene carbonate (EC) and dimethyl carbonate (DMC). Cyclic voltammetry was carried out using an Autolab (Ecochemie, Pgstat 30) electrochemical workstation. The same apparatus was used to record the electrochemical impedance spectra in the frequency range 0.1 Hz to 500 kHz at a disturbance amplitude of 10 mV. Galvanostatic measurements were performed on an Arbin BT2143 in a voltage range of 0.0 to 3.0 V at various currents (1 C is defined as 372 mA·g^{-1}). To block electromagnetic fields, the cells were located inside a Faraday cage.

3 Results and discussion

The pristine material, that is, the WYS, is amorphous since no reflections appeared in its XRD pattern. Structural information was obtained from the sodium oleate for comparison (Fig. S1 in the Electronic Supplementary Material (ESM)). The similarity of the spectra is evident, which is indicative of a very similar structure dominated by the presence of the oleate anion. The change of cation would be responsible for slight variations in the vibration frequencies of the different peaks of the spectra. Therefore, reflux heating essentially maintained the structure of

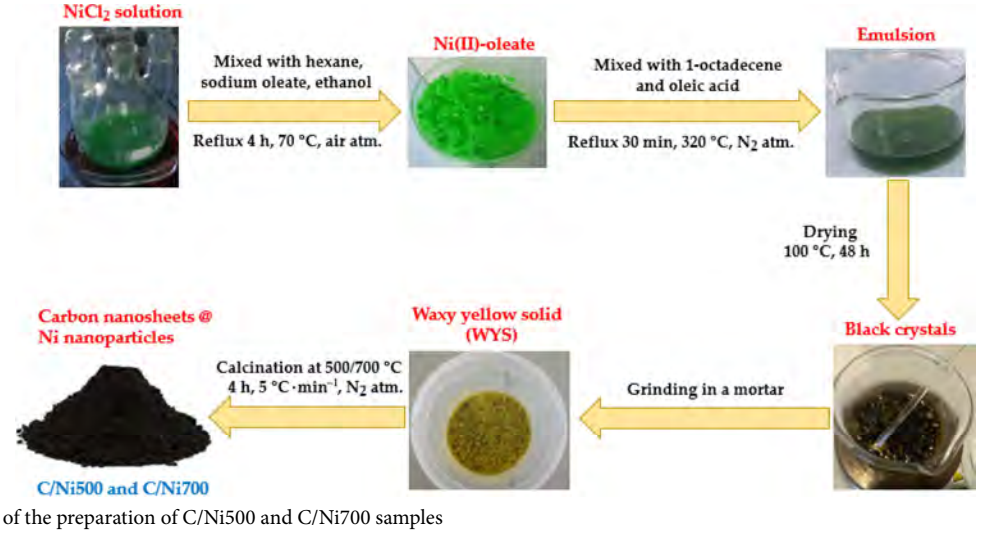

Figure 1 Scheme of the preparation of C/Ni500 and C/Ni700 samples

the Ni complex and its decomposition into Ni and/or NiO is not appreciated. Hence the need to carry out the pyrolysis of the material and identify the resulting products.

To accurately determine the appropriate temperatures at which to carry out the pyrolysis process, the thermogravimetric (TG) curve was recorded in N_2 atmospheres. This curve is shown in Fig. S2 in the ESM and the TG curve of sodium oleate has been included for comparison. The thermal decomposition of this last salt takes place in a single step, between 400 and 500 °C. The remaining residue is around 17%, a value consistent with the formation of Na_2CO_3 according to the global reaction (1)

$$C_{18}H_{33}O_2Na + \Delta Q\ (\text{at. } N_2) \rightarrow Na_2CO_3(s) + H_2(g) + CO(g) + \text{hydrocarbon gases} \quad (1)$$

The formation of this salt involves different redox reactions. The identification of gases produced requires the use of thermobalance functions such as IR, gas chromatography or mass spectrometry. However, our equipment lacks these functions. Thermal decomposition of the Ni complex starts around 170 °C and takes place in two steps. The first step ends around 300 °C and a 46% weight is lost. Thermal decomposition of pure $Ni(OA)_2$ [10, 11] virtually occurs in a single step and both the temperature and the weight loss are notably higher. The second weight loss takes place between 300 and 470 °C and accounts for an additional 50%. The total weight loss is somewhat higher than that of $Ni(OA)_2$. It seems plausible that the two steps of the thermogravimetric curve are related to the presence of oleic acid. The confirmation of this hypothesis would require knowledge of the nature of the gases released and/or the identification by XRD of intermediates formed, and these are out of our reach. Hence, the interest of TG measurements resides in the ability to find the decomposition temperature of the material to select the temperatures for the pyrolysis. Two temperatures were selected: 500 °C, where the organic component of the material was almost completely lost, and 700 °C, with a heating time of 4 h.

The XRD patterns of the samples obtained after heating at 500 and 700 °C are shown in Fig. 2. Reflections at 44.80, 52.00, and 76.70° 2θ the spacing values appear in both diffractograms, coincident with those of the planes (111), (200) and (220) of Ni metal in a face-centred cubic structure (PDF #03-1051). These results are in good agreement with those obtained by Xiao et al. [11] but differ from the data reported by Kim et al. [10] in which the hexagonal phase grows at the expense of the cubic phase with increasing temperature. For the sample pyrolyzed at 700 °C, a well-defined, symmetric and somewhat broadened peak is observed at 26.5 and two very weak at 43.1° and 54.3° 2θ. All these peaks are consistent with the graphite structure (PDF #25-0284). The strong peak is assigned to the (002)

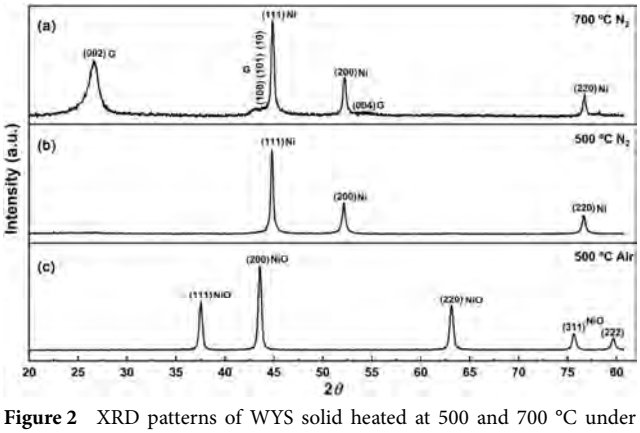

Figure 2 XRD patterns of WYS solid heated at 500 and 700 °C under different atmospheres.

plane; the weak peak at 44.1° 2θ, which overlaps with the (111) Ni plane, is produced by several planes, the most intense being (100), (010), and (101); finally, the (004) plane is also discernible. On the other hand, when the treatment in N_2 atmosphere is carried out at 500 °C, only the peak corresponding to the plane (002) is barely perceptible. Temperature is too low to achieve a graphitic ordering of the carbon particles. Therefore, the C formed under these conditions is virtually amorphous. After heating at 500 °C under air atmosphere, the only phase detected was NiO, Fig. 2(c).

Although the main application of the XRD pattern of a polycrystalline material is to obtain information of its structure and composition, information on the microstructure can be found from the peak broadening. Specifically, the so-called crystallite size can be evaluated, defined as the size of a region of the crystal that diffracts X-rays coherently. The formula to evaluate the above quantity is the Scherrer equation

$$D = K\lambda/(\beta\cos(\theta))$$

where D is the crystallite size, K is a constant that depends on the shape of the crystals (it has been taken to be 0.9), λ is the wavelength of the X-rays (CuKα_1 1.54 Å), β is the full width half maximum of the peak (in radians) once the instrumental widening has been subtracted and θ is the Bragg angle. Lanthanum hexaboride, LaB_6, a compound obtained at high temperatures and with a high crystallinity, was the reference standard used to correct the width of the peaks. The values of crystallite size for the two phases detected, Ni and C, are shown in Table 1. These correspond to nanometric species. Regarding Ni, for which the two most intense planes have been used to evaluate the crystallite size, the values obtained for each peak are very similar, which is indicative of its isotropic character.

The morphology of C/Ni500 and C/Ni700 samples was analysed by transmission electron microscopy (TEM). Images at different magnifications of the C/Ni500 sample are shown in Fig. 3. The nanocrystals of Ni present a strong tendency to agglomerate (Fig. 3(a)), which makes it difficult to specify their real size. As the magnification increases (Fig. 3(b)) one can observe the morphology of the nanoparticles to be rather irregular with a size around 10 nm. These images show that the nanocrystals are stuffed in an amorphous matrix formed by the carbonaceous skeleton from the pyrolysis of the organic component of the material, in good agreement with the amorphous structure revealed by XRD (Fig. 2).

When heating at 700 °C in N_2 atmosphere, the agglomerates are no longer observed, and the particles appear more dispersed (Fig. 4(a)), encapsulated in a matrix more transparent to electrons such as carbon. The morphology of Ni nanocrystals is more homogeneous, with a tendency to adopt a pseudospherical shape. Their size is in between 10 and 30 nm, in good agreement with that obtained from the XRD broadening analysis (Table 1). Regarding the graphitized C that covers the Ni nanoparticles, the planes (002) of spacing 0.33 nm are clearly observed (Fig. 4(b)), in good agreement with the reflection of the same plane observed in the XRD pattern, Fig. 2. The value of the crystallite size of 10 nm along <001> direction would mean that the carbon sheets approximately contain 30 layers of C atoms (10/0.33). The spherical morphology of the Ni nanoparticles controls the growth

Table 1 Crystallite size of the Ni and C in C/Ni700 sample

	Plane	D (nm)
Ni	(111)	24
	(200)	25
C	(002)	10

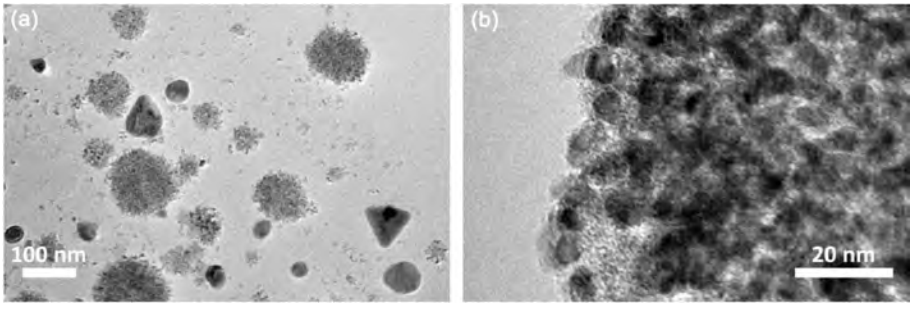

Figure 3 TEM images of C/Ni500 sample recorded at different magnifications.

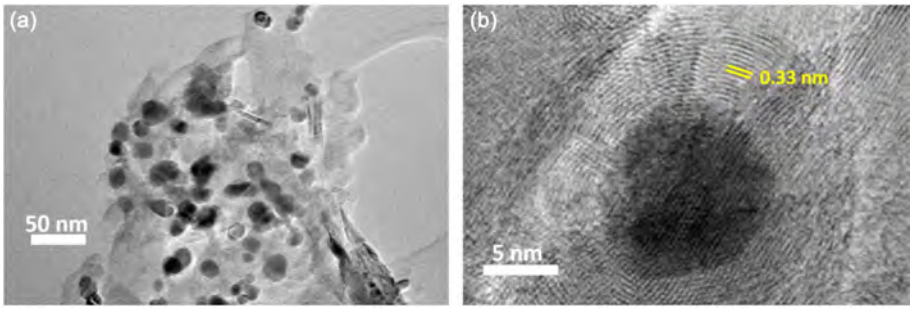

Figure 4 TEM images of C/Ni700 samples recorded at different magnifications.

of the carbonaceous matrix causing the curvature of the carbon layers. The graphitization of chemically derived graphene sheets has been studied by Long et al. [20] by heating at very high temperatures, 2,800 °C. Under these conditions, they also observed structural arrangements of the 2D graphene sheets that lead to the formation of loops on the tip of graphene sheets, like those shown in Fig. 4(b) and Fig. S3 in the ESM. The role of the Ni nanoparticles as effective catalyst for improving the degree of graphitization of the carbon matrix graphitization is clearly visible, drastically reducing the graphitization temperature.

The amorphous structure of the C of sample C/Ni500 is confirmed by the HRTEM image shown in Fig. S4 in the ESM. It is worth noting that the absence of fringes associated with the planes (002) of the graphite compared to the image of the sample C/Ni700, Fig. 4(b), in which the ordering of the planes is clearly observed. The lattice fringes observed exhibit *d*-spacing of 0.21 nm which is consistent with the spacing of the (111) planes of Ni, in good agreement with the crystalline character deduced from the XRD pattern (Fig. 2). Several causes can justify the difficulty of observing the crystalline nature of the Ni nanoparticles obtained at 700 °C, such as an increase in its thickness and a more effective coating by the carbon matrix along with its greater degree of graphitization.

For the study of the electrochemical properties of these Ni/C composites in Li cells, the C/Ni700 sample was chosen owing to the greater degree of graphitization of the C compared with C/Ni500 sample. For this reason, we have made complementary measurements to know its composition and the texture and structure of the surface. This last property has been analysed by XPS. The survey spectrum (Fig. S5(a) in the ESM) shows the C 1s photoemission as the peak of greatest intensity followed by the O 1s and Ni 2p photoemission peaks, this later element indiscernible in the survey spectrum (see Table 2, Fig. S5(a) in the ESM).

Table 2 Atomic concentration (%) of C/Ni700 sample obtained from the XPS spectrum

C	O	Ni
97.36	2.44	0.20

The C 1s spectrum was fitted to five components (Fig. 5) [21, 22], whose contributions and their binding energies are shown in Table 3. The main contributions correspond to –C–C–, –C=C– and adventitious carbon. The low relative intensity contributions at higher binding energies were assigned to C–O, C=O, O–C=O groups at 286.3, 287.6, and 289.5 eV, respectively, and the contribution at 291.5 eV to a satellite peak due to π→π* transition. The Ni 2p photoemission peak is barely detected (Fig. S5(b) in the ESM, Table 2). This result is quite surprising since a technique like XPS, particularly sensitive to the first layers

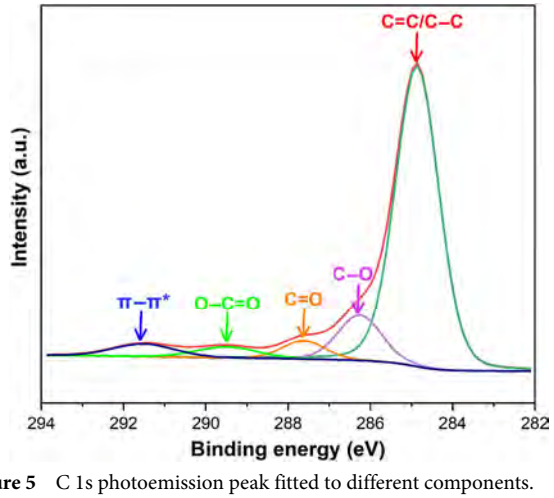

Figure 5 C 1s photoemission peak fitted to different components.

Table 3 Contribution of the five components used in the fitting of the C 1s core level signal and BE. The C/O ratio is also included

C 1s	BE (eV)	Area (%)
C=C/–C–C–	284.8	75.46
C–O	286.3	11.49
C=O	287.6	4.60
O–C=O	289.5	3.91
π→π*	291.5	4.54
C/O	—	97.36/2.44

of atoms, should have more clearly identified the presence of the element, which was done by XRD. A convincing explanation of this outcome can be drawn from the HRTEM images, Fig. 4(b), in which it is shown that Ni nanocrystals are covered with a layer of carbon thick enough to shield them from photoelectrons. Not only does the XPS technique reflect the efficient encapsulation of the Ni nanocrystals by the carbon sheets but also the HCl treatment confirmed this unexpected behaviour. The Ni nanocrystals withstood the attack with this acid at 80 °C for 12 h.

The Raman spectrum (Fig. S6 in the ESM) exhibits a strong peak at 1,580 cm^{-1} corresponding to the in-plane stretching mode of graphite (G peak). The presence of disorder in the graphitic lattice is revealed by other characteristics [23], such as a peak at around 1,350 cm^{-1} (D band). The peaks at 2,700 cm^{-1} correspond to the first overtone of the D band (G′ or 2D). The overtone 2D band has been used for obtaining information on the number of layers and on the stacking order in carbon systems [23]. Its broadening is consistent with there being more than five graphene stacked layers [24].

The textural properties were examined from the N_2 adsorption–desorption isotherm shown in Fig. S7 in the ESM, the shape of which lies in between type II and IV, the latter suggested by the small hysteresis loop caused by the formation of a mesopore system. The surface area calculated from the adsorption curve via the Brunauer–Emmett–Teller (BET) method was 88 $m^2 \cdot g^{-1}$ and the pore volume was found to be 0.14 $cm^3 \cdot g^{-1}$. The carbon content in the C/Ni composite was obtained from TG measurements taken under oxygen atmosphere, Fig. S8 in the ESM. Starting at about 420 °C, a slight weight loss is observed. At temperatures above 500 °C, such loss increases abruptly until it stabilizes at around 79%. This weight loss corresponds to the carbon content in the composite as the reaction which occurs is (2)

$$C/Ni(s) + O_2(g) \rightarrow NiO(s) + CO_2(g) \quad (2)$$

The Ni content calculated after conversion into NiO is 21%, much higher than that measured by XPS. This result confirms the effective coating exerted by carbon on Ni nanocrystals, which in practice prevents photoionization.

The satisfactory crystallinity of the carbon sheets and their efficient ability to encapsulate the Ni nanoparticles, whose presence should lead to an improvement in the conductive properties of the composite, are solid arguments to encourage the study of their electrochemical properties and their use as electrodes for Li-ion batteries. In order to verify this assumption, the electrochemical properties of the composite in Li half-cells have been studied by measurements of cyclic voltammetry, impedance and galvanostatic charge/discharge cycling. The cyclic voltammetry curves of the first three cycles are shown in Fig. 6(a). Their shape matches well with that of other carbons previously reported [25–27]. Two cathodic peaks can be observed during the first lithiation process. The first one, broad and well-defined, appears below 1 V and is attributed to the formation of a solid electrolyte interface (SEI) on the surface of the carbon nanosheets (CNS) [28–30]. The peak is enhanced by the low particle size and the structural disorder of the CNS. The second peak, located below 0.2 V, is caused by the intercalation of Li within the interlayer spacing of the CNS. On charging the cell, a strong peak defines the Li deintercalation process, but its slowness, brought about by the rupture of the strong bonds of the Li atoms and the lattice defects, polarizes the cell and the oxidation process appears at slightly higher voltages [26]. A very weak oxidation peak is observed at around 0.9 V, attributable to a limited reversibility of the SEI process. The next two cyclic voltammetry (CV) curves show very similar profiles, but there are appreciable differences compared with the first cathodic scan. The cathodic peak assigned to the electrolyte reduction resulting in the SEI formation is hardly detectable. A very weak cathodic peak appears between 0.2 and 0.1 V, the origin of which suggests a small change in the Li intercalation mechanism after the first discharge/charge curve. The anodic scans maintain their shape and the only change is the decrease in the intensity of the deintercalation peak when going from the first to the second charge.

The impedance spectra of the Li cell recorded under open circuit conditions (OCV) and after the CV measurements are shown in Fig. 6(b). A change in the shape of the Nyquist plot of the cells is observed at high/medium frequency in the form of one and two depressed semicircles at OCV and after cycling, respectively. This modification is attributed to the SEI formation clearly reflected in the first reduction scan (see Fig. 6(a)). At low frequency, the plots show the typical inclined line attributed to the lithium diffusion process within the carbon electrode. The EIS data of the cycled cell was fitted to a Randles equivalent circuit with three components: R_e (electrolyte resistance), R_{SEI} and C_{SEI}, the resistance and capacitance of the SEI, respectively, C_{dl} together with R_{ct}, the double layer capacitance and charge transfer resistance and Z_w, the Warburg impedance related to the diffusion of Li ions in the composite. A similar Randles circuit has been used to fit the data of the cell at OCV, eliminating the component attributed to the SEI formation. The results of the analysis are collected in Table 4. The data reveal a remarkably low interphase resistance which decreases from 126.65 to 19.00 Ω upon CV, behaviour frequently observed [31, 32]. Its origin must be ascribed to the SEI formation due to reduction of the electrolyte, film that plays an outstanding role in the electrochemical reaction of the electrode [33]. Its ionic nature is a key property to facilitate and maintain the Li ion transfer process between the electrodes when the cell is cycled. Its kinetics is governed by the charge transfer resistance [34]. A

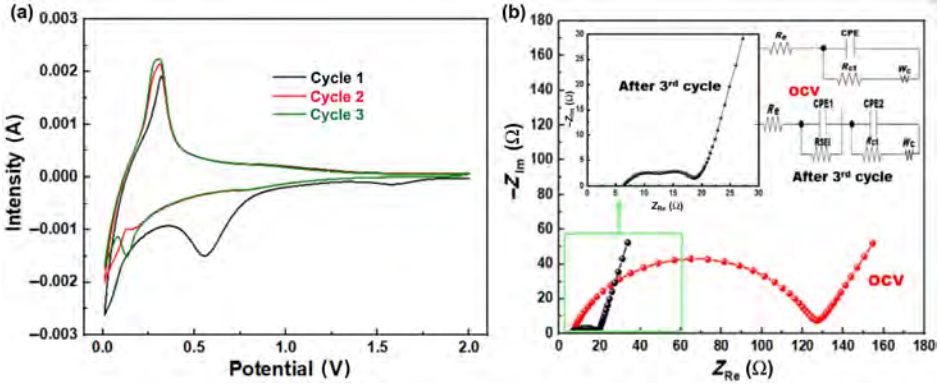

Figure 6 (a) CV curves. (b) EIS spectra of the electrode made from C/Ni700 sample. The equivalent circuits used to fit the spectra are shown.

Table 4 Values of the different resistances calculated from the impedance spectra (Fig. 6(b))

Resistances	OCV	After CV
R_e (Ω)	6.56	6.4
R_{SEI} (Ω)	—	7.32
R_{ct} (Ω)	120	5.28
$R = R_e + R_{SEI} + R_{ct}$ (Ω)	126.65	19.00
χ^2	6.6×10^{-5}	4.8×10^{-5}

decrease in the R_{ct} accelerates the electrode reaction kinetics. This is reflected in an enhancement of the reversibility of the electrochemical reaction and a better maintenance of the capacity as a result. Values significantly higher than those measured for our composite have been found for electrodes based on natural graphite [35], graphene nanosheets [36], hierarchical porous carbons [37], carbon nanocages [38] and single wall carbon nanotubes [39], among others. The lower resistance observed in the carbon nanosheets/Ni composite nanoparticles is attributed to the presence of Ni metal whose electrical conductivity would result in an increase in the overall conductivity of the composite.

Some of the discharge/charge curves recorded at 0.25 C rate (93 mA·g^{-1}) are shown in Fig. 7. The first discharge curve exhibits a rapid drop in the potential, followed by a pseudo plateau between 0.8 and 0.7 V and a smoother decrease of the potential until 0.0 V is reached. The capacity released in the different processes undergone by the electrode was about 1,190 mAh·g^{-1}. When charging the cell, a slight polarization is observed, followed by a sharp rise in the potential and a subtle change in slope around 1 V. The capacity calculated at the 3 V cut-off point was 780 mAh·g^{-1}. Two clear differences between both curves are worth noting, the virtual disappearance of the plateau in the charge curve and a decrease of the capacity around 410 mAh·g^{-1} (irreversible capacity, IC). This capacity loss is attributed to different factors, some well-known as the reaction of Li with the electrolyte to form a passive layer called SEI and others more difficult to characterize such as electrolyte reduction reactions associated with functional groups (O,H) or absorbed species resulting from exposure to air after pyrolysis [40–42]. The presence of defects depending on the degree of carbon graphitization as well as high specific surface values also increase the irreversible capacity loss [43]. The pseudo-plateau disappears in the second and subsequent discharge curves while the potential decreases smoothly from 1 V. The charge curves hardly change as the cell is cycled. The discharge/charge profiles of this carbon are more similar to those of graphitized carbons [44] than to those of more disordered carbons, among other graphenes and carbon nanotubes [45, 46]. In these carbons, a strong polarization is observed between the discharge and charge curves and an abnormally high irreversible capacity as a result.

The values of specific capacity as a function of the number of cycles are shown in the Fig. 8. The average value after 50 cycles was of 723 mAh·g^{-1}, almost twice the theoretical capacity of graphite. By increasing the current density at 1 C, a pronounced decrease in the capacity released by the electrode was observed. The average value is around 205 mAh·g^{-1} after 200 cycles (see inset in Fig. 8). The rate capability measurements confirmed a progressive drop in the capacity of the electrode, more pronounced in the interval ranging from 0.1 to 0.6 C (Fig. 9). The average capacity values calculated were 855, 553, 360, 210, 135, and 80 mAh·g^{-1} at 0.1, 0.3, 0.6, 1, 2, and 3 C, respectively. When the current is restored to 0.1 C, the electrode recovers most of its capacity, around 815 mAh·g^{-1}. SEM measurements of the electrode of this cell before and after cycling supplied valuable information of one of the causes of its outstanding capacity recovery: the maintenance and improvement of the morphological and textural properties of the composite in the deposit. The SEM image before cycling, Fig. S9(a) in the ESM, reveals a porous texture of the deposit, well adapted for an effective impregnation by the electrolyte. After cycling, Fig. S9(b) in the ESM, the deposit becomes more compact, improving the contact between particles. Moreover, the electrode barely suffers deterioration as revealed by the absence of composite-free area.

To examine the influence of the mass loading on the electrode performance, a deposit with a carbon loading of 6.4 mg·cm^{-2}

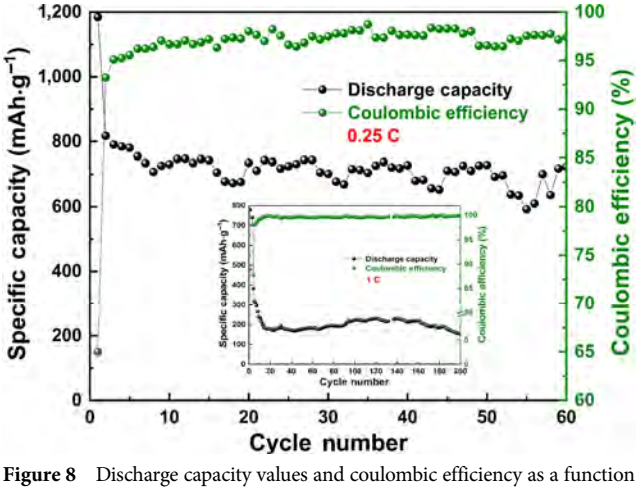

Figure 8 Discharge capacity values and coulombic efficiency as a function of the cycle number for C/Ni700 electrode at 0.25 C rate. The inset shows the cycling properties at 1 C rate.

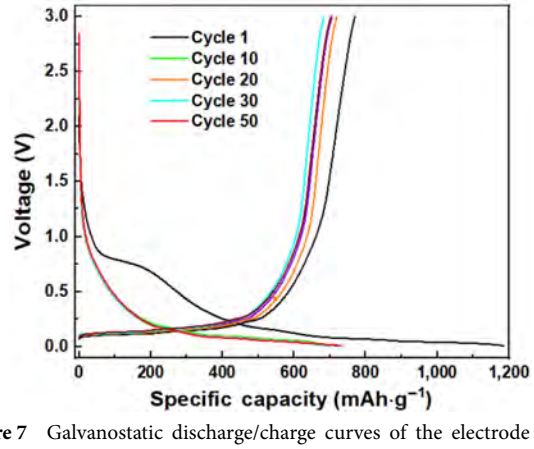

Figure 7 Galvanostatic discharge/charge curves of the electrode made from C/Ni700 sample recorded at 0.25 C.

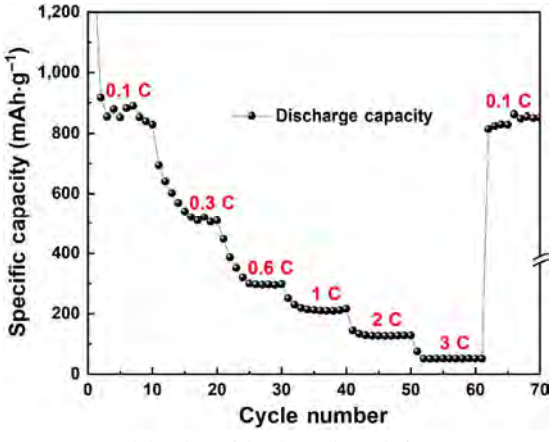

Figure 9 Rate capability data of the electrode made from C/Ni700 sample.

was prepared and only 5% of binder and 5% of CB. Although in the first cycle the specific capacity of this electrode gave relatively low values, Fig. S10 in the ESM, around 675 mAh·g^{-1}, probably associated with the cell not yet stabilized, in the 2nd cycle the delivered capacity increases appreciably, 1,069 mAh·g^{-1}. Then, a discontinuous decrease in capacity was observed in the 20 cycles measured. The average value is around 800 mAh·g^{-1}, somewhat higher than that measured for the electrode with lower carbon loading. As for the coulombic efficiency values, after the first cycle the values tend to normalize and reach values slightly below 100%. The good electrochemical response when increasing the C loading is attributed to the presence of Ni and its contribution to the improvement of composite conductivity.

Changes in the structural properties of the composite components after cycling were examined by *ex-situ* measurements of XRD diffraction and TEM images. The XRD pattern of the electrode after seven cycles is shown in Fig. S11 in the ESM. The cycled composite exhibits the three Ni peaks as well as uncycled (see Fig. 2(a)), a direct proof that the chemical status of Ni during Li cycling processes remains unchanged. On the other hand, the graphite peak corresponding to the plan (002) virtually disappears, suggesting the collapse of its structure and a tendency to amorphize. The high-resolution TEM (HRTEM) images are consistent with these results. In many areas of the grid the ordering of the graphite planes has been lost (see Fig. S12(a) in the ESM). There are some areas where graphite crystallographic planes are still observed with a significant disorder (Fig. S12(b) in the ESM), indicative of the amorphization process that the carbon undergoes during the charge and discharge of the cell. In this image a Ni nanoparticle, magnified in Fig. S12(c) in the ESM, is observed in which the ordering of the planes (111) is hardly affected, reflecting the electrochemical inactivity of the element against Li metal and in good agreement with the XRD pattern shown in Fig. S11 in the ESM.

The effectiveness of carbon nanosheets/Ni nanoparticles composite for Li-ion batteries can be analysed by establishing a comparison with the observed behaviour for other nanocarbon-based systems reported in the literature, Table 5. Most of these carbons are highly disordered as revealed by the low intensity, high broadening and asymmetry of the (002) peak. To make this comparison more reliable, the following properties have been collected: specific surface area (S_{BET}), irreversible capacity (IC), polarization between the discharge and charge curves (ΔV), and cycling properties including rate capability data. The polarization data have been calculated taking as a reference the value of the average capacity of the cycles reported. Regarding the number of cycles, the adopted criterion has been to select fifty cycles, value at which the electrode has reached a satisfactory stability. Generally, the loss of initial capacity increases with the degree of disorder and the specific surface of the nanostructured carbon. Especially striking is the behaviour of carbon nanospheres obtained from chloroform at low temperatures (80 °C) but using potassium as reducing agent [45]. This carbon delivers the highest capacity but presents serious drawbacks such as high values of irreversible capacity and polarization in addition to the explosive nature of the potassium element. The value of the irreversible capacity of the mesoporous graphene studied by Jiao et al. [16], obtained by a similar synthetic methodology used here but based on Fe_3O_4 nanocrystals, further removed by HCl, is abnormally high. It does not seem that the high value of the specific surface is responsible for this behaviour, since no correlation is observed between both properties. In contrast, this carbon has a high polarization value, a property that shows a clearer relationship with the irreversible capacity. Regarding the performance of our carbon compared with nanostructured synthetic carbons, it is worth highlighting its good performance at relatively low values of current density. In fact, it delivers much higher capacity values. On the other hand, it also has a relatively low polarization value between the charge and discharge curve as well as a moderate irreversible loss of capacity. All these properties make it attractive as an electrode for Li-ion batteries. For higher current densities, the composite presents a significant decrease in capacity, but it has good capacity retention on cycling and coulombic efficiency values close to 100% after the

Table 5 Selected properties of Li/ion half-cells made from different nanostructured carbons reported in literature

Preparation method	S_{BET} ($m^2 \cdot g^{-1}$)	IC ($mAh \cdot g^{-1}$)	Cycling properties			Rate cap.		Ref.
			ΔV (V)	rate (C)	$C_{50\ cycles}$ ($mAh \cdot g^{-1}$)	Rate (C)	Capacity ($mAh \cdot g^{-1}$)	
Hollow carbon spheres: template-based synthesis, heating temperature 700 °C, highly disordered	970	960	—	—	—	0.2 1.0	600 400	[47]
Hollow carbon nanospheres: hydrothermal treatment, (550 °C), highly disordered	270	985	1.1	0.1	600	0.5 1 2	409 337 229	[48]
Hydrogenated carbon nanospheres: hydrothermal treatment (80 °C), highly disordered	43	2,500	1.5	0.13	978	—	—	[49]
Hierarchical porous carbon: template synthesis, heating temperature 900 °C, highly disordered	254	430	0..6	—	—	0.1 0.2 0.4	210 190 130	[37]
Carbon nanocages: highly disordered	—	570	0.8	0.25 0.80	520 410	—	—	[38]
Ordered mesoporous few layers graphene framework: heating temperature 500 °C, highly disordered	1,000	1,678	1.6	0.8 1.6*	400 180*	0.8 1.6 3.2	520 430 320	[12]* [16]
Graphitic oxide exfoliated at 800 °C, highly disordered	45	488	0.5	0.2 1	290 200	—	—	[50]
Graphene like graphite: thermal treatment of graphitic oxide at 800 °C, less disordered	31	400	—	—	—	0.1 0.5 1	372 350 325	[51]
Carbon nanosheets with embedded Ni nanocrystals: heating temperature 700 °C, less disordered	88	410	0.2	0.25 1	723 205	0.1 0.3 0.6 1	855 553 360 210	This work

first cycles. Nevertheless, as remarked above the shortcoming in the capacity fall is partly mitigated by its behaviour in the rate capability test, that is, the outstanding recovery of the high capacity when lower current densities are restored. We do not want to ignore the good rate capabilities of the ordered mesoporous graphene sheets reported in Ref. [16], synthesized by a method that presents several stages like the one used in this work. However, the low intensity values of the CV curves strike us, these being an order of magnitude lower than those of our composite. A few months earlier, the same group studied in Li batteries a mesoporous carbon synthesized by the same method and in conditions like Ref. [12]. The values of the capacity obtained at 1.6 C and 50 cycles were only 180 $mAh \cdot g^{-1}$, closer to those found in this work.

4 Conclusions

In summary, a nanostructured carbon highly graphitized embedded with disperse Ni nanocrystals, synthesized via a thermolysis route, is a good candidate to act as anode for Li-ion batteries. It exhibits a very satisfactory performance by maintaining a specific capacity higher than 700 $mAh \cdot g^{-1}$ when it cycles at a current density of 100 $mA \cdot g^{-1}$. Although at higher current densities the delivered capacity decreases, the high values are recovered when a lower rate is restored. There are several causes to explain this good behaviour. The existence of a highly conductive phase such as Ni nanocrystals significantly reduces the resistance of the electrode. In the first cycles, the charge-transfer resistance barely reaches 5 Ω, which enhances the charge carrier mobility and the reversibility of the Li intercalation/de-intercalation reaction. The high carbon graphitization results in small polarization values between the charge and discharge curve, which significantly reduce the irreversible capacity. These are relevant properties to maintain a similar performance when acting as anodes in real Li-ion cells (full cell configuration).

Acknowledgements

This research was funded by Ministerio de Economía y Competitividad (No. MAT2017-87541-R) and Junta de Andalucía (Group FQM-175). F. J. S. gratefully acknowledges UCO for fellowship "Universidad de Córdoba. Becas Semillero de Investigación". E. R. C. thanks to project RTI2018-099668-BC22 of Ministerio de Ciencia, Innovación y Universidades, and project UMA18-FEDERJA-126 of Junta de Andalucía and FEDER funds. J. C. V. also acknowledges financial Support from UCLM through the 2019-GRIN-27165 grant.

Electronic Supplementary Material: Supplementary material (IR spectra, TG curves, SEM, HREM and TEM images, XPS survey, Raman spectrum, N_2 isotherms) is available in the online version of this article at https://doi.org/10.1007/s12274-019-2576-4.

References

[1] Weller, H. Colloidal Semiconductor Q-Particles: Chemistry in the transition region between solid state and molecules. *Angew. Chem., Int. Ed.* **1993**, *32*, 41–53.

[2] Alivisatos, A. P. Semiconductor clusters, nanocrystals, and quantum dots. *Science* **1996**, *271*, 933–937.

[3] Tao, Y. S.; Kanoh, H.; Abrams, L.; Kaneko, K. Mesopore-modified zeolites: Preparation, characterization, and applications. *Chem. Rev.* **2006**, *106*, 896–910.

[4] Hyeon, T. Chemical synthesis of magnetic nanoparticles. *Chem. Commun.* **2003**, 927–934.

[5] Lewis, E.; Haigh, S.; O'Brien, P. The synthesis of metallic and semiconducting nanoparticles from reactive melts of precursors. *J. Mater. Chem. A* **2014**, *2*, 570–580.

[6] Park, J.; An, K.; Hwang, Y.; Park, J. G.; Noh, H. J.; Kim, J. Y.; Park, J. H.; Hwang, N. M.; Hyeon, T. Ultra-large-scale syntheses of monodisperse nanocrystals. *Nat. Mater.* **2004**, *3*, 891–895.

[7] Jana, N. R.; Chen, Y. F.; Peng, X. G. Size- and shape-controlled magnetic (Cr, Mn, Fe, Co, Ni) oxide nanocrystals via a simple and general approach. *Chem. Mater.* **2004**, *16*, 3931–3935.

[8] Kim, Y. H.; Kang, Y. S.; Lee, W. J.; Jo, B. G.; Jeong, J. H. Synthesis of Cu nanoparticles prepared by using thermal decomposition of Cu-oleate complex. *Mol. Cryst. Liq. Cryst.* **2006**, *445*, 231/[521]–238/[528].

[9] Bao, N. Z.; Shen, L. M.; Wang, Y.; Padhan, P.; Gupta, A. A Facile thermolysis route to monodisperse ferrite nanocrystals. *J. Am. Chem. Soc.* **2007**, *129*, 12374–12375.

[10] Kim, S. G.; Terashi, Y.; Purwanto, A.; Okuyama, K. Synthesis and film deposition of Ni nanoparticles for base metal electrode applications. *Colloid. Surf. A Physicochem. Eng. Asp.* **2009**, *337*, 96–101.

[11] Xiao, Q. F.; Sohn, H.; Chen, Z.; Toso, D.; Mechlenburg, M.; Zhou, Z. H.; Poirier, E.; Dailly, A.; Wang, H. Q.; Wu, Z. B. et al. Mesoporous metal and metal alloy particles synthesized by aerosol-assisted confined growth of nanocrystals. *Angew. Chem., Int. Ed.* **2012**, *51*, 10546–10550.

[12] Jiao, Y. C.; Han, D. D.; Ding, Y.; Zhang, X. F.; Guo, G. N.; Hu, J. H.; Yang, D.; Dong, A. G. Fabrication of three-dimensionally interconnected nanoparticle superlattices and their lithium-ion storage properties. *Nat. Commun.* **2015**, *6*, 6420.

[13] Buck, M. R.; Biacchi, A. J.; Schaak, R. E. Insights into the thermal decomposition of Co(II) oleate for the shape-controlled synthesis of Wurtzite-type CoO nanocrystals. *Chem. Mater.* **2014**, *26*, 1492–1499.

[14] Bau, J. A.; Li, P.; Marenco, A. J.; Trudel, S.; Olsen, B. C.; Luber, E. J.; Buriak, J. M. Nickel/Iron oxide nanocrystals with a nonequilibrium phase: Controlling size, shape, and composition. *Chem. Mater.* **2014**, *16*, 4796–4804.

[15] Behera, B. C.; Ravindra, A. V.; Padhan, P. Structural phase transformation of nickel nanostructures with synthetic approach conditions. *J. Appl. Phys.* **2014**, *115*, 17B510.

[16] Jiao, Y. C.; Han, D. D.; Liu, L. M.; Ji, L.; Guo, G. N.; Hu, J. H.; Yang, D.; Dong, A. G. Highly ordered mesoporous few-layer graphene frameworks enabled by Fe3O4 nanocrystal superlattices. *Angew. Chem., Int. Ed.* **2015**, *54*, 5727–5731.

[17] Yu, H. J.; Li, H. W.; Yuan, S. Y.; Yang, Y. C.; Zheng, J. H.; Hu, J. H.; Yang, D.; Wang, Y. G.; Dong, A. G. Three-dimensionally ordered, ultrathin graphitic-carbon frameworks with cage-like mesoporosity for highly stable Li-S batteries. *Nano Res.* **2017**, *10*, 2495–2507.

[18] Han, D. D.; Jiao, Y. C.; Han, W. Q.; Wu, G. H.; Li, T. T.; Yang, D.; Dong, A. G. A molecular-based approach for the direct synthesis of highly-ordered, homogeneously-doped mesoporous carbon frameworks. *Carbon* **2018**, *140*, 265–275.

[19] Xu, S. H.; Zhang, F. Y.; Kang, Q.; Liu, S. H.; Cai, Q. Y. The effect of magnetic field on the catalytic graphitization of phenolic resin in the presence of Fe–Ni. *Carbon* **2009**, *47*, 3233–3237.

[20] Long, D. H.; Li, W.; Qiao, W. M.; Miyawaki, J.; Yoon, S. H.; Mochida, I.; Ling, L. C. Graphitization behaviour of chemically derived graphene sheets. *Nanoscale* **2011**, *3*, 3652–3656.

[21] Abouimrane, A.; Compton, O. C.; Amine, K.; Nguyen, S. T. Non-annealed graphene paper as a binder-free anode for lithium-ion batteries. *J. Phys. Chem. C* **2010**, *114*, 12800–12804.

[22] Vargas, Ó.; Caballero, Á.; Morales, J.; Rodríguez-Castellón, E. Contribution to the understanding of capacity fading in graphene nanosheets acting as an anode in full li-ion batteries. *ACS Appl. Mater. Interfaces* **2014**, *6*, 3290–3298.

[23] Bokobza, L.; Bruneel, J. L.; Couzi, M. Raman spectroscopy as a tool for the analysis of carbon-based materials (highly oriented pyrolitic graphite, multilayer graphene and multiwall carbon nanotubes) and of some of their elastomeric composites. *Vibrat. Spectros.* **2014**, *74*, 57–63.

[24] Ferrari, A. C.; Meyer, J. C.; Scardaci, V.; Casiraghi, C.; Lazzeri, M.; Mauri, F.; Piscanec, S.; Jiang, D.; Novoselov, K. S.; Roth, S. et al. Raman spectrum of graphene and graphene layers. *Phys. Rev. Lett.* **2006**, *97*, 187401.

[25] Courtel, F. M.; Niketic, S.; Duguay, D.; Abu-Lebdeh, Y.; Davidson, I. J. Water-soluble binders for MCMB carbon anodes for lithium-ion batteries. *J. Power Sources* **2011**, *196*, 2128–2134.
[26] Ding, F.; Xu, W.; Choi, D.; Wang, W.; Li, X. L.; Engelhard, M. H.; Chen, X. L.; Yang, Z. G.; Zhang, J. G. Enhanced performance of graphite anode materials by AlF3 coating for lithium-ion batteries. *J. Mater. Chem.* **2012**, *22*, 12745–12751.
[27] Zhao, D. D.; Wang, L.; Yu, P.; Zhao, L.; Tian, C. G.; Zhou, W.; Zhang, L.; Fu, H. G. From graphite to porous graphene-like nanosheets for high rate lithium-ion batteries. *Nano Res.* **2015**, *8*, 2998–3010.
[28] Yao, J.; Wang, G. X.; Ahn, J. H.; Liu, H. K.; Dou, S. X. Electrochemical studies of graphitized mesocarbon microbeads as an anode in lithium-ion cells. *J. Power Sources* **2003**, *114*, 292–297.
[29] Hasa, I.; Hassoun, J.; Passerini, S. Nanostructured Na-ion and Li-ion anodes for battery application: A comparative overview. *Nano Res.* **2017**, *10*, 3942–3969.
[30] Gao, M. Y.; Liu, N. Q.; Chen, Y. L.; Guan, Y. P.; Wang, W. K.; Zhang, H.; Wang, F.; Huang, Y. Q. An *in situ* self-developed graphite as high capacity anode of Lithium-ion Batteries. *Chem. Commun.* **2015**, *51*, 12118–12121.
[31] Carbone, L.; Coneglian, T.; Gobet, M.; Munoz, S.; Devany, M.; Greenbaum, S.; Hassoun, J. A simple approach for making a viable, safe, and high-performances lithium sulfur battery. *J. Power Sources* **2018**, *377*, 26–35.
[32] Luna-Lama, F.; Hernández-Rentero, C.; Caballero, A.; Morales, J. Biomass-derived carbon/γ-MnO_2 nanorods/S composites prepared by facile procedures with improved performance for Li/S batteries. *Electrochim. Acta* **2018**, *292*, 522–531.
[33] Peled, E.; Menkin, S. Review-SEI: Past, present and future. *J. Electrochem. Soc.* **2017**, *164*, A1703–A1719.
[34] Zhang, S. S. Effect of discharge cutoff voltage on reversibility of lithium/sulfur batteries with $LiNO_3$-contained electrolyte. *J. Electrochem. Soc.* **2012**, *159*, A920–A923.
[35] Wang, L.; Zhao, J. S.; He, X. M.; Ren, J. G.; Zhao, H. P.; Gao, J.; Li, J. J.; Wan, C. R.; Jiang, C. Y. Investigation of modified nature graphite anodes by electrochemical impedance spectroscopy. *Int. J. Electrochem. Sci.* **2012**, *7*, 554–560.
[36] Guo, P.; Song, H. H.; Chen, X. H. Electrochemical performance of graphene nanosheets as anode material for lithium-ion batteries. *Electrochem. Commun.* **2009**, *11*, 1320–1324.
[37] Yi, J.; Li, X. P.; Hu, S. J.; Li, W. S.; Zhou, L.; Xu, M. Q.; Lei, J. F.; Hao, L. S. Preparation of hierarchical porous carbon and its rate performance as anode of lithium ion battery. *J. Power Sources* **2011**, *196*, 6670–6675.
[38] Li, G. D.; Xu, L. Q.; Hao, Q.; Wang, M.; Qian, Y. T. Synthesis, characterization and application of carbon nanocages as anode materials for high-performance lithium-ion batteries. *RSC Adv.* **2012**, *2*, 284–291.
[39] Ng, S. H.; Wang, J.; Guo, Z. P.; Chen, J.; Wang, G. X.; Liu, H. K. Single wall carbon nanotube paper as anode for lithium-ion battery. *Electrochim. Acta* **2005**, *51*, 23–28.
[40] Xue, J. S.; Dahn, J. R. Dramatic effect of oxidation on lithium insertion in carbons made from epoxy resins. *J. Electrochem. Soc.* **1995**, *142*, 3668–3677.
[41] Buiel, E.; Dahn, J. R. Reduction of the irreversible capacity in hard-carbon anode materials prepared from sucrose for Li-ion Batteries. *J. Electrochem, Soc.* **1998**, *145*, 1977–1981.
[42] Hu, Y. S.; Adelhelm, P.; Smarsly, B. M.; Hore, S.; Antonietti, M.; Maier, J. Synthesis of hierarchically porous carbon monoliths with highly ordered-microstructure and their application in rechargeable lithium batteries with high-rate capability. *Adv. Funct. Mater.* **2007**, *17*, 1873–1878.
[43] Arrebola, J. C.; Caballero, A.; Hernán, L.; Morales, J.; Olivares-Marín, M.; Gómez-Serrano, V. Improving the performance of biomass-derived carbons in Li-ion batteries by controlling the lithium insertion process. *J. Electrochem. Soc.* **2010**, *157*, A791–A797.
[44] Arrebola, J. C.; Caballero, A.; Hernán, L.; Morales, J. Graphitized carbons of variable morphology and crystallinity: A comparative study of their performance in lithium cells. *J. Electrochem. Soc.* **2009**, *156*, A986–A992.
[45] Cai, X. Y.; Lai, L. F.; Shen, Z. X.; Lin, J. Y. Graphene and graphene-based composites as Li-ion battery electrode materials and their application in full cells. *J. Mater. Chem. A* **2017**, *5*, 15423–15446.
[46] Landi, B. J.; Ganter, M. J.; Cress, C. D.; DiLeo, R. A.; Raffaelle, R. P. Carbon nanotubes for lithium ion batteries. *Energy Environ. Sci.* **2009**, *2*, 638–654.
[47] Yang, S. B.; Feng, X. L.; Zhi, L. J.; Cao, Q.; Maier, J.; Müllen, K. Nanographene-constructed hollow carbon spheres and their favorable electroactivity with respect to lithium storage. *Adv. Mater.* **2010**, *22*, 838–842.
[48] Han, F. D.; Bai, Y. J.; Liu, R.; Yao, B.; Qi, Y. X.; Lun, N.; Zhang, J. X. Template-free synthesis of interconnected hollow carbon nanospheres for high-performance anode material in lithium-ion batteries. *Adv. Energy Mater.* **2011**, *1*, 798–801.
[49] Xiao, J. P.; Yao, M. G.; Zhu, K.; Zhang, D.; Zhao, S. J.; Lu, S. C.; Liu, B.; Cui, W.; Liu, B. B. Facile synthesis of hydrogenated carbon nanospheres with a graphite-like ordered carbon structure. *Nanoscale* **2013**, *5*, 11306–11312.
[50] Vargas C, O. A.; Caballero, Á.; Morales, J. Can the performance of graphenenanosheets for lithium storage in Li-ion batteries be predicted? *Nanoscale* **2012**, *4*, 2083–2092.
[51] Cheng, Q.; Okamoto, Y.; Tamura, N.; Tsuji, M.; Maruyama, S.; Matsuo, Y. Graphene-like-graphite as fast-chargeable and high-capacity anode materials for lithium ion batteries. *Sci. Rep.* **2017**, *7*, 14782.

Table of contents

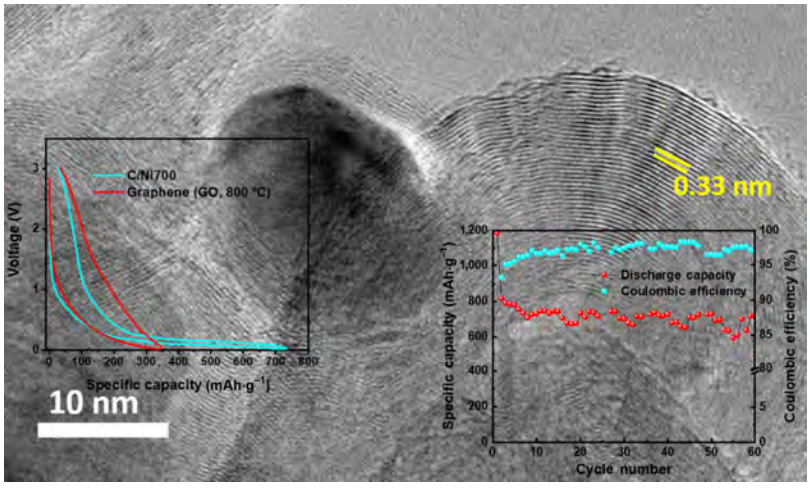

A graphitized carbon@Ni nanocrystals composite obtained at moderate temperatures possesses the ability of doubling the capacity of graphite with a similar polarization between the charge and discharge curves, much lower than that of disordered graphene.

Electronic Supplementary Material

Highly graphitized carbon nanosheets with embedded Ni nanocrystals as anode for Li-ion batteries

Francisco Javier Soler-Piña[1], Celia Hernández-Rentero[1], Alvaro Caballero[1] (✉), Julián Morales[1] (✉), Enrique Rodríguez-Castellón[2], and Jesús Canales-Vázquez[3]

[1] *Dpto. Química Inorgánica e Ingeniería Química, Instituto de Química Fina y Nanoquímica, Universidad de Córdoba, 14071 Córdoba, Spain*
[2] *Dpto. Química Inorgánica, Cristalografía y Mineralogía, Facultad de Ciencias, Universidad de Málaga, 29071 Málaga, Spain*
[3] *Instituto de Energías Renovables, Universidad de Castilla-La Mancha, Paseo de La Investigación 1, 02071 Albacete, Spain*

Supporting information to https://doi.org/10.1007/s12274-019-2576-4

ELECTRONIC SUPPLEMENTARY MATERIAL. Figure S1: IR spectra for sodium oleate and waxy yellow solid. Figure S2: TG curves of Na-oleate and the waxy yellow solid recorded under N_2 atmosphere. Figure S3: HRTEM image of several types of loops defined by the different number of graphite layers. Figure S4: HRTEM image of C/Ni500 sample. Observe the amorphous and crystalline nature of C and Ni, respectively. Figure S5: (a) Survey XPS spectrum of C/Ni700 sample (b) Photoemission signal in the Ni 2p region. Figure S6: Raman spectrum of C/Ni700 sample. Figure S7: N_2 adsorption/desorption curve of C/Ni700 sample. Figure S8: TG curve of the C/Ni700 sample recorded under O_2 atmosphere. Figure S9: SEM images. (a) The pristine electrode made from C/Ni700 sample. (b) After the rate capability test (see Fig. 9). Figure S10: Discharge capacity values and coulombic efficiency as a function of the cycle number for C/Ni700 electrode at 0.25C. Carbon loading: 6.4 mg cm^{-2}. Figure S11: XRD pattern of the electrode made from C/Ni700 sample after 7 cycles (cut off at the discharge state). Figure S12: HRTEM images of the electrode made from C/Ni700 sample after 7 cycles (cut off at the discharge state). (a) Amorphized carbon nanosheets. (b) Highly disordered carbon nanosheets; yellow circle: Ni nanoparticle. (c) Ni nanoparticle observed in (b) and magnified; the ordering of the (111) planes of Ni is clearly observed.

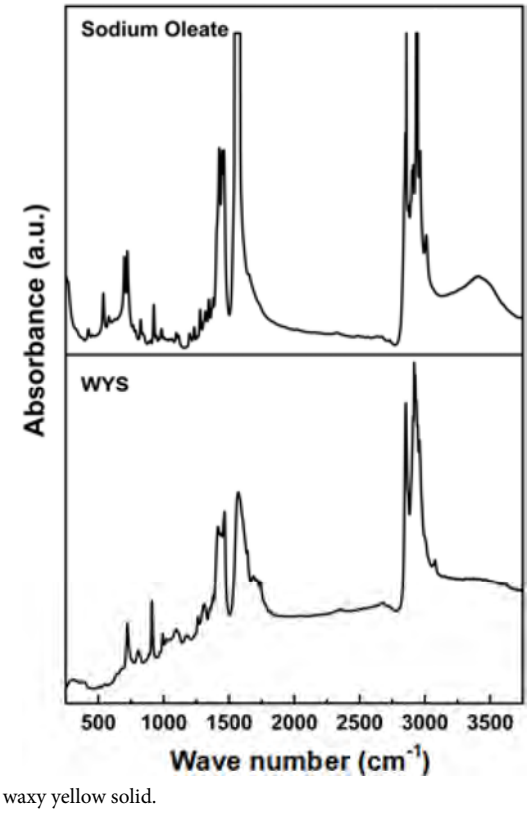

Figure S1 IR spectra for sodium oleate and waxy yellow solid.

Address correspondence to Alvaro Caballero, alvaro.caballero@uco.es; Julián Morales, iq1mopaj@uco.es

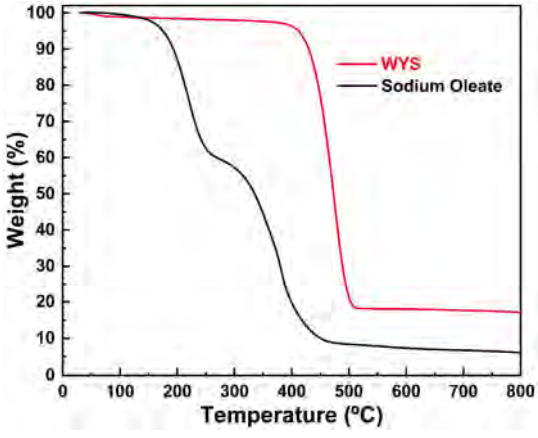

Figure S2 TG curves of Na-oleate and the waxy yellow solid recorded under N_2 atmosphere.

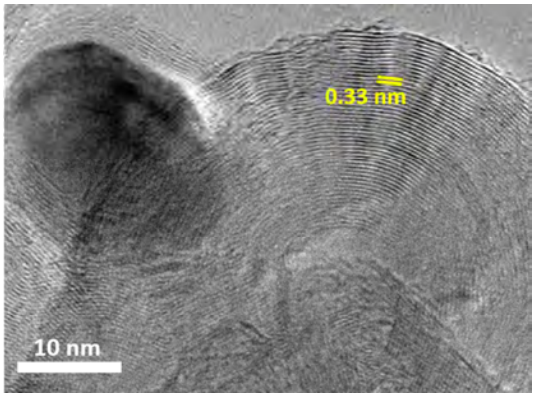

Figure S3 HRTEM image of several types of loops defined by the different number of graphite layers.

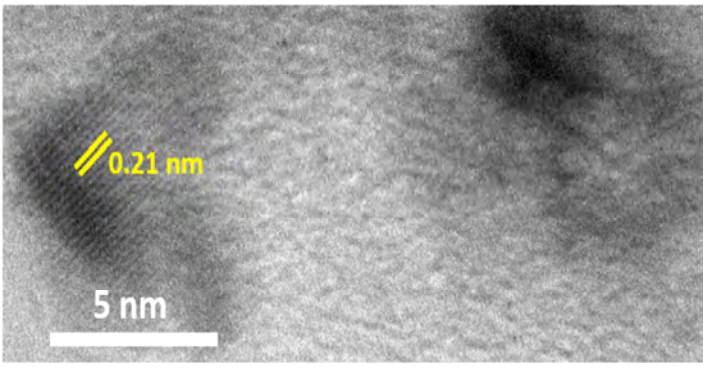

Figure S4 HRTEM image of C/Ni500 sample. Observe the amorphous and crystalline nature of C and Ni, respectively.

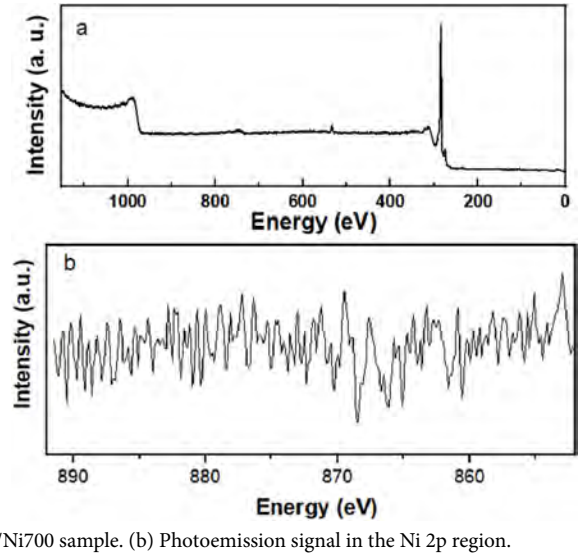

Figure S5 (a) Survey XPS spectrum of C/Ni700 sample. (b) Photoemission signal in the Ni 2p region.

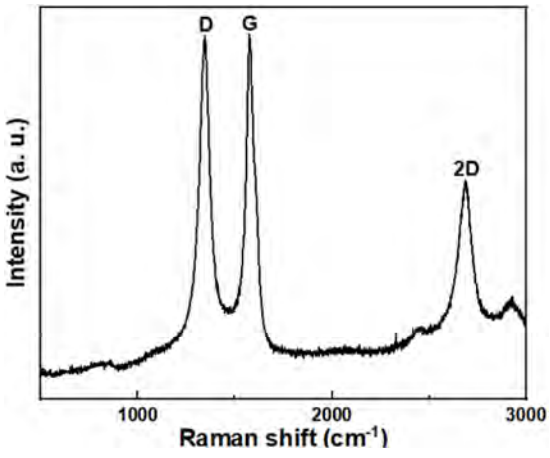

Figure S6 Raman spectrum of C/Ni700 sample.

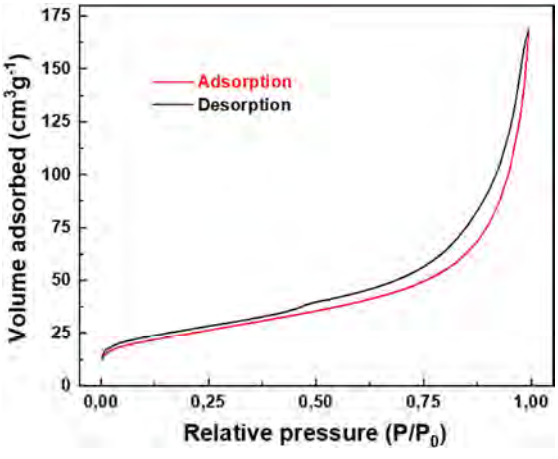

Figure S7 N_2 adsorption/desorption curve of C/Ni700 sample.

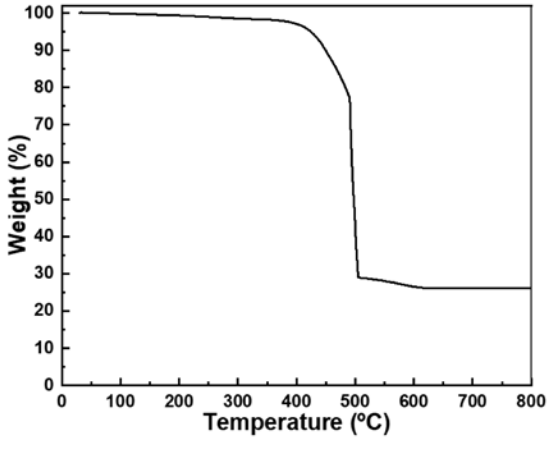

Figure S8 TG curve of the C/Ni700 sample recorded under O_2 atmosphere.

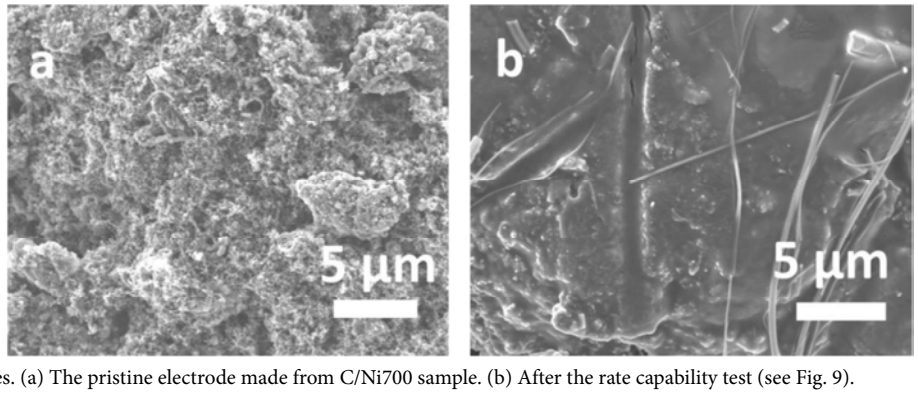

Figure S9 SEM images. (a) The pristine electrode made from C/Ni700 sample. (b) After the rate capability test (see Fig. 9).

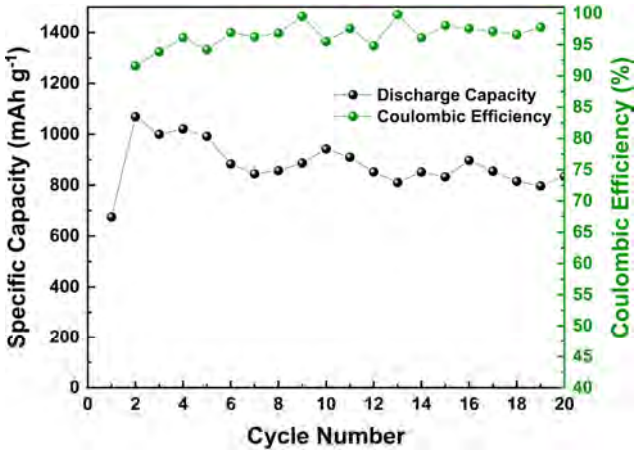

Figure S10 Discharge capacity values and coulombic efficiency as a function of the cycle number for C/Ni700 electrode at 0.25C. Carbon loading: 6.4 mg cm^{-2}.

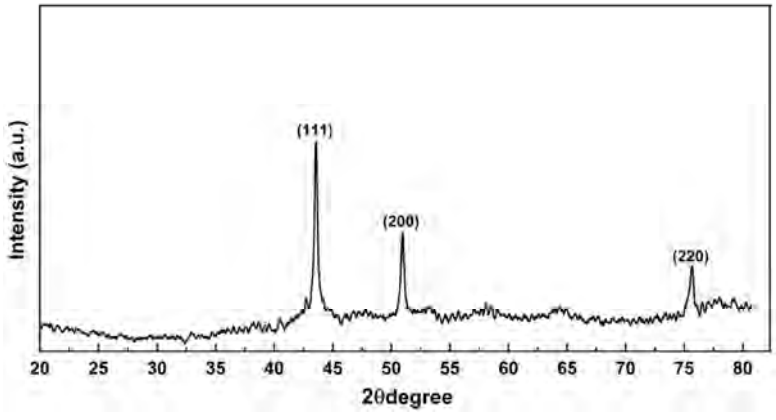

Figure S11 XRD pattern of the electrode made from C/Ni700 sample after 7 cycles (cut off at the discharge state).

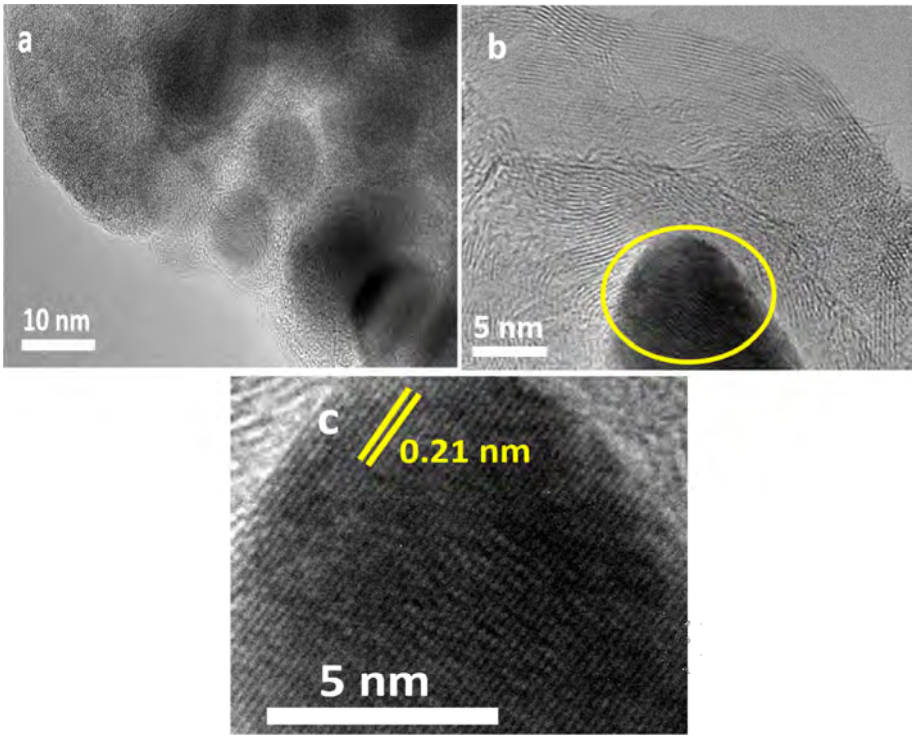

Figure S12 HRTEM images of the electrode made from CNi700 sample after 7 cycles (cut off at the discharge state). (a) Amorphized carbon nanosheets. (b) Highly disordered carbon nanosheets; yellow circle: Ni nanoparticle. (c) Ni nanoparticle observed in (b) and magnified; the ordering of the (111) planes of Ni is clearly observed.